Approach to criticality in the fragmentation of xenon by 1–19 GeV protons

N. T. Porile, A. J. Bujak, D. D. Carmony, Y. H. Chung,* L. J. Gutay, A. S. Hirsch, M. Mahi, G. L. Paderewski,† T. C. Sangster,‡ R. P. Scharenberg, and B. C. Stringfellow
Department of Physics and Department of Chemistry, Purdue University, West Lafayette, Indiana 47907
(Received 20 May 1988)

Differential cross sections for the emission of intermediate-mass fragments ($3 \leq Z_f \leq 14$) at 48.5° and 131.5° in the interaction of xenon with 1–19 GeV protons have been measured. The excitation functions rise sharply with energy up to ~10 GeV and then level off. The energy spectra were fitted with an expression based on the phase transition droplet model. Excellent fits with reasonable parameters were obtained for $E_p \geq 9$ GeV. Below 6 GeV, the fits show an increasing contribution with decreasing energy from another mechanism, believed to be binary breakup. A droplet model fit to the cross sections ascribed to the multifragmentation component is able to reproduce the variation of the yields with both fragment mass and proton energy. The results are interpreted in terms of the phase diagram of nuclear matter.

I. INTRODUCTION

The emission of intermediate-mass fragments (IMF) in reactions induced by energetic protons and heavy ions has been a subject of recent interest. In a study of IMF emission in the interaction of 80–350 GeV protons with krypton and xenon, we reported that the fragment mass yield distribution obeys a power law, $\sigma(A_f) \propto A_f^{-2.6}$ (Ref. 1). Since clustering according to a power law with an exponent of 2.0–2.5 is displayed by many systems near their critical point,[2–4] we proposed that fragment formation could be viewed in analogy to the density fluctuations and clustering expected in a liquid-gas system near its critical point. The successful description of the isotopic and isobaric fragment yield distributions[5–8] by an adaptation of Fisher's one-component droplet model[9] lent further credence to this hypothesis. Additional experimental support has been provided by Warwick *et al.*,[10] who showed that IMF emission in the interaction of relativistic projectiles involves a multibody breakup process. Fragment emission has been treated theoretically in the context of the liquid-gas phase transition by a number of authors.[11–15] Alternative explanations of some of the data on the basis of multiparticle phase-space calculations, rate equation estimates, dynamical calculations, fast breakup models, and percolation models have also been given.[16–29]

Our previous experiment on IMF emission was performed in the limiting fragmentation energy regime. It is known from radiochemical experiments[30,31] that the cross sections for IMF production by protons begin to decrease as the bombarding energy decreases below 10–20 GeV towards an effective threshold of several hundred MeV. Furthermore, significant changes in mechanism occur at these lower energies. For example, the angular distributions change from forward-peaked at energies up to a few GeV to sideward-peaked above 10 GeV,[32,33] and the energy spectra show a concomitant broadening and shift towards lower energies, particularly for heavy IMF from heavy-element targets.[34] These observations make it of interest to examine IMF production in the context of the liquid-gas phase transition at energies below 20 GeV where other mechanisms, such as binary breakup, presumably also contribute to IMF production.

Relatively few measurements of IMF energy spectra have been reported for incident protons below 20 GeV. Poskanzer and collaborators[35–37] have reported results at 5 GeV for silver and uranium targets. More recently, Korteling and coworkers[38,39] studied IMF production in the interaction of silver with 0.2–0.5 GeV protons. We report here the results of an experiment on IMF production in the interaction of xenon with 1–19 GeV protons performed in the internal beam of the Brookhaven Alternating Gradient Synchrotron (AGS). We used a xenon gas jet target, a technique we first employed to study IMF production at Fermilab.[6,40] This technique is ideally suited to study the evolution of IMF production with increasing energy in the near-threshold regime because results can be obtained over a nearly continuous range of energies. Preliminary reports of our results have been published elsewhere.[41–43]

II. EXPERIMENTAL

The experimental procedure has been described in detail in a previous report.[44] Briefly, the experiment was mounted in a 2.5 m long straight section of the AGS. The gas jet target consisted of a xenon-hydrogen mixture containing 1% or 3% xenon. Typically, the jet was fired for 50 ms during each AGS acceleration cycle, sampling a 2–4 GeV/c wide beam momentum interval. The interval limits could be moved between 2 and 20 GeV/c by adjusting the start of the jet pulse relative to beam injection. The gas inlet pressure was set at 25 psi (gauge). Approximately 80% of the gas in the jet was collected in a 1000 L buffer volume maintained at high vacuum by two unbaffled 5600 L/s oil diffusion pumps. The remaining gas was pumped away by additional pumps attached to the target box and in differential pumping chambers lo-

cated between the target box and the main ring. Small amounts of gas entering the main ring were removed by the AGS pumps. The target box pressure increased to a peak value of 4×10^{-6} Torr between beam pulses. An automatic gate valve interlock system was installed in order to isolate the main ring from the experimental apparatus in case of a sudden vacuum failure.

The target thickness was found to be $(2.5\pm0.2)\times10^{15}$ atoms/cm^2 ($\sim$15 ng/cm^2) and the FWHM of the jet in the interaction region was 11.8±0.1 mm. These values were based on the number of recoil protons from *p-p* elastic scattering with the hydrogen component detected in two ΔE-E-Veto silicon surface barrier monitor telescopes located at 84.8° to the beam. The various detectors were chosen to cover a proton energy range of 5–19 MeV in one telescope and 8–28 MeV in the other, values that span the range of recoil energies expected for interactions with 2–20 GeV/c protons. The monitor telescopes were also used to optimize the radial position of the jet relative to the beam. This was accomplished by determining the recoil proton count rate as a function of the jet radial position and choosing the position yielding the maximum rate. These jet scans were usually performed after the weekly AGS maintenance shutdowns and whenever the bombarding energy interval was changed.

Two identical telescopes, mounted at 48.5° and 131.5° to the beam, were used to measure the energy spectra of elementally resolved fragments with atomic number in the $Z_f=3-14$ range.[45] The telescopes consisted of a Frisch grid ionization chamber backed by a silicon surface barrier E detector. Fragments entered the ionization chamber through an unsupported 80 μg/cm^2 polypropylene window, (Ref. 46) 1.9 cm in diameter. The pressure inside the ionization chamber was maintained at 20 Torr by a flow of P-10 counting gas. The silicon detector had an active area of 300 mm^2, which provided a solid angle of $\sim2.1\times10^{-5}$ sr, and was 1 mm thick. The performance of the detectors was monitored with ^{241}Am α-particle sources mounted inside the ion chambers and with pulsers. The chambers could be isolated from the main ring by gate valves connected to the automatic interlock system. Small adjustments to the telescope centerlines could be made remotely in order to ensure that the detectors viewed the region of maximum beam-jet interaction. These telescope scans were performed following the adjustments in the jet position mentioned above.

The electronics and data acquisition system are described in detail elsewhere.[47] The acquisition program was a modified version of the code SNAP.[48] Event information was written onto magnetic tape for subsequent off-line analysis. We detected approximately 10^6 fragments with $Z\geq3$ during five months of data taking.

The analysis of the data involved the charge identification of the IMF on the basis of the usual band separation obtained in ΔE versus E plots. Fragment energies were corrected for energy losses in detector windows and for pulse height defect in the silicon detector. The number of observed fragments of given charge and energy was corrected for multiple scattering losses.[6] Differential cross sections were obtained relative to the *p-p* elastic cross section on the basis of the number of protons detected in the monitor telescopes. Protons observed in these telescopes were separated from other $Z=1$ and $Z=2$ particles on the basis of the ΔE-E measurements. The proton energy spectra were fitted with a Gaussian representing the elastic component and an empirical background function representing inelastic protons originating in interactions with xenon. The final IMF results were binned into 11 incident proton energy intervals spanning the 1.3–19.1 GeV range. The interval limits are given in Table I.

III. RESULTS

Typical fragment energy spectra are displayed in Fig. 1. The low-energy cutoff arises from detector thresholds and energy losses in the foils preceding the detectors. The curves through the data are the result of a thermal model fit, described in Sec. IV A. These curves were used to estimate the unmeasured portions of the spectra, thereby permitting the determination of the differential cross sections. The unmeasured contribution increased from approximately 3% of the total for Li fragments to $\sim$40% for Si fragments. The values of $d\sigma/d\Omega$ are tabulated in Table I. The quoted errors are statistical and are based on the number of events in both fragment and monitor telescopes. The uncertainties in the estimate of the yields of low-energy fragments are believed to be $\sim$10%, contributing uncertainties of 0.3–4% to the overall differential cross sections. The systematic variation with fragment Z of the Coulomb parameters in the thermal fits, which are determined primarily by the low-energy region of the spectra, confirms that these uncertainties cannot be large. Systematic errors are $\sim$25% and are comprised chiefly of the uncertainty in the alignment of the telescopes with the jet/beam interaction region and of the uncertainty in the uniformity of the gas jet mixture.

Figure 2 shows the dependence on mass and proton energy of the differential cross sections obtained at 48.5°. Qualitatively similar results are obtained at 131.5°. In making this plot the fragment atomic numbers were converted to average mass numbers on the basis of the isotopic yields of IMF previously obtained by us in *p*-Xe collisions at Fermilab.[6] The values of the cross-section weighted average mass numbers $\langle A_f \rangle$ corresponding to given charges Z_f are listed in Table I. The fragment yields in Fig. 2 increase with decreasing mass number as well as with increasing proton energy. The increase with energy is particularly pronounced at the lower energies; the cross sections are nearly constant above 10 GeV.

The differential cross sections are shown in further detail in Fig. 3, which displays the excitation functions of Li-O fragments. The points at 80 GeV are from our previous Fermilab experiment.[6] Although the Fermilab data were obtained at 34°, the flatness of the fragment angular distributions from medium mass targets at forward angles[40,49] makes it reasonable to compare the two sets of data. The Fermilab cross sections are in good agreement with the higher energy AGS values, showing that an internal gas jet target can indeed yield reliable results

TABLE I. Differential cross sections for the emission of fragments in p-Xe interactions.

Z_f	$\langle A_f \rangle$	E_p (GeV) / $d\sigma/d\Omega$[a]	1.3–2.0	2.0–2.7	2.7–3.4	3.4–4.1
3	7.04		1.321±0.110[b]	2.289±0.197	3.537±0.303	4.818±0.413
4	9.04		0.543±0.046	1.040±0.090	1.645±0.142	2.323±0.200
5	11.09		0.495±0.042	0.977±0.085	1.590±0.137	2.210±0.191
6	12.82		0.383±0.033	0.790±0.069	1.299±0.112	1.849±0.160
7	15.10		0.208±0.019	0.471±0.042	0.803±0.070	1.146±0.100
8	17.06		0.142±0.013	0.310±0.028	0.570±0.050	0.838±0.074
9	19.66		0.0892±0.0087	0.224±0.021	0.362±0.033	0.527±0.048
10	21.58		0.0819±0.0081	0.205±0.019	0.370±0.033	0.541±0.049
11	23.72		0.0729±0.0074	0.178±0.017	0.312±0.029	0.480±0.044
12	25.70		0.0706±0.0072	0.163±0.016	0.319±0.029	0.423±0.039
13	27.96		0.0458±0.0051	0.121±0.012	0.271±0.025	0.390±0.037
14	30.81		0.0461±0.0051	0.117±0.012	0.269±0.025	0.370±0.035
3	7.04		0.571±0.048[c]	1.056±0.091	1.688±0.145	2.313±0.198
4	9.04		0.255±0.022	0.530±0.046	0.786±0.068	1.086±0.094
5	11.09		0.253±0.022	0.515±0.045	0.805±0.070	1.159±0.101
6	12.82		0.205±0.018	0.436±0.038	0.680±0.059	0.957±0.083
7	15.10		0.119±0.011	0.256±0.023	0.421±0.037	0.589±0.052
8	17.06		0.0775±0.0075	0.171±0.016	0.298±0.027	0.425±0.038
9	19.66		0.0484±0.0050	0.105±0.010	0.184±0.017	0.284±0.026
10	21.58		0.0490±0.0051	0.114±0.011	0.184±0.017	0.297±0.027
11	23.72		0.0372±0.0041	0.0946±0.0094	0.165±0.016	0.273±0.026
12	25.70		0.0436±0.0046	0.0948±0.0094	0.154±0.015	0.262±0.025
13	27.96		0.0475±0.0050	0.0651±0.0068	0.143±0.014	0.186±0.018
14	30.81		0.0297±0.0035	0.0798±0.0082	0.119±0.012	0.188±0.019

4.1–4.9	4.9–5.6	8.7–10.1	10.1–11.4	14.0–15.1	15.1–16.2	17.1–19.1
5.854±0.503	7.562±0.919	11.421±0.692	11.453±0.695	13.158±0.790	13.876±0.834	12.830±0.781
2.875±0.249	3.744±0.458	5.218±0.324	5.339±0.331	6.265±0.381	6.475±0.394	6.150±0.384
2.786±0.242	3.661±0.448	4.998±0.310	5.067±0.315	5.884±0.359	6.196±0.378	5.706±0.357
2.250±0.196	2.963±0.364	4.069±0.255	4.178±0.262	4.909±0.301	5.178±0.317	4.661±0.295
1.424±0.126	1.798±0.223	2.517±0.164	2.663±0.173	3.080±0.193	3.203±0.201	2.893±0.191
1.024±0.092	1.198±0.151	1.718±0.115	1.866±0.124	2.225±0.142	2.248±0.144	2.061±0.140
0.649±0.060	0.774±0.099	1.128±0.080	1.179±0.084	1.458±0.096	1.428±0.095	1.283±0.093
0.672±0.061	0.835±0.107	1.144±0.081	1.157±0.082	1.346±0.090	1.381±0.093	1.316±0.096
0.572±0.054	0.720±0.093	0.915±0.067	0.939±0.069	1.150±0.079	1.158±0.080	0.907±0.071
0.545±0.052	0.697±0.091	0.945±0.070	0.804±0.061	1.105±0.076	1.100±0.077	0.952±0.074
0.465±0.045	0.464±0.062	0.704±0.055	0.755±0.059	0.877±0.063	0.913±0.066	0.694±0.058
0.449±0.044	0.545±0.073	0.671±0.054	0.612±0.050	0.924±0.066	0.844±0.062	0.641±0.055
2.137±0.185	3.053±0.373	5.887±0.360	6.215±0.379	6.644±0.391	6.885±0.406	4.785±0.295
1.285±0.113	1.472±0.182	3.023±0.190	3.084±0.194	3.421±0.208	3.618±0.220	3.316±0.208
1.339±0.118	1.530±0.189	2.977±0.189	3.177±0.201	3.542±0.215	3.923±0.238	3.737±0.235
1.153±0.102	1.335±0.166	2.528±0.161	2.725±0.173	2.957±0.177	3.081±0.185	3.129±0.198
0.736±0.067	0.815±0.103	1.621±0.107	1.697±0.112	1.928±0.119	1.960±0.121	2.074±0.135
0.496±0.046	0.575±0.074	1.201±0.081	1.196±0.081	1.347±0.085	1.371±0.087	1.427±0.096
0.335±0.032	0.364±0.049	0.777±0.056	0.806±0.058	0.865±0.058	0.908±0.061	0.892±0.064
0.393±0.037	0.375±0.050	0.790±0.057	0.868±0.062	0.880±0.059	0.915±0.062	0.895±0.064
0.271±0.027	0.359±0.048	0.652±0.049	0.609±0.047	0.759±0.052	0.770±0.054	0.782±0.058
0.311±0.030	0.314±0.043	0.591±0.045	0.587±0.045	0.747±0.052	0.771±0.054	0.685±0.052
0.209±0.022	0.195±0.028	0.557±0.044	0.573±0.044	0.649±0.046	0.616±0.045	0.682±0.053
0.263±0.027	0.259±0.036	0.495±0.040	0.491±0.040	0.620±0.045	0.707±0.051	0.557±0.045

[a]Differential cross sections in mb/sr.
[b]$\theta_{lab} = 48.5°$.
[c]$\theta_{lab} = 131.5°$.

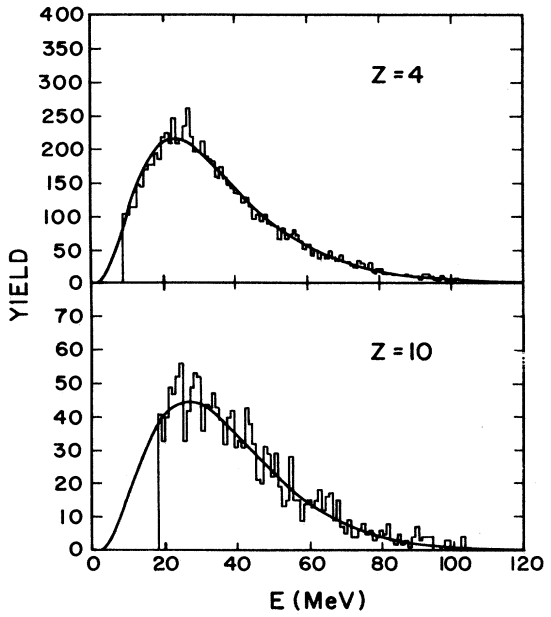

FIG. 1. Energy spectra of Be and Ne fragments emitted at 48.5° to the beam in p-Xe interactions. The proton energy interval is 10.1–11.4 GeV. The curves are the result of a thermal model fit described in the text.

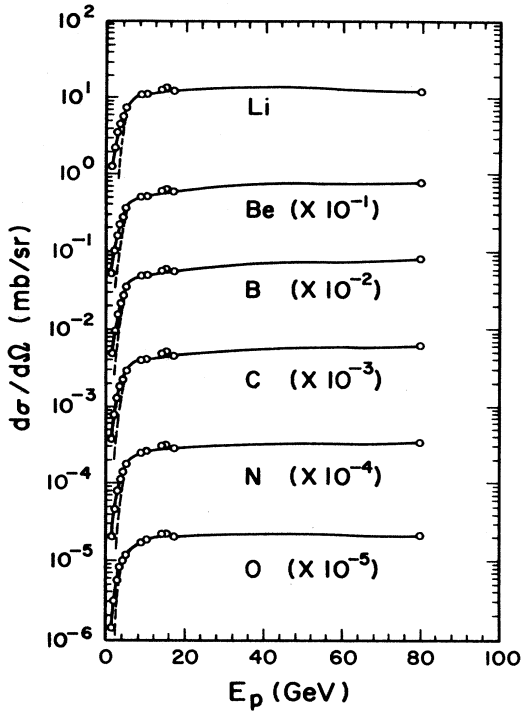

FIG. 3. Excitation functions for Li-O fragments emitted at 48.5° to the beam. The point at 80 GeV is taken from the Fermilab experiment (Ref. 6). The dashed curves below 6 GeV represents the contribution of the multifragmentation mechanism.

that are independent of the vastly different beam profiles at the two accelerators.

Figure 4 shows the energy dependence of the ratio of differential cross sections at 48.5° and 131.5° for Be and O fragments. The forward-backward ratios go through a maximum in the vicinity of 5 GeV and tend to decrease with increasing fragment charge. The observed energy dependence is qualitatively similar to that exhibited by numerous forward-backward emission ratios of fragmentation and deep spallation products,[31,50,51] and may reflect a similar change in angular distribution as seen in the experiments cited above,[32,33] i.e., from forward- to sideward-peaked.

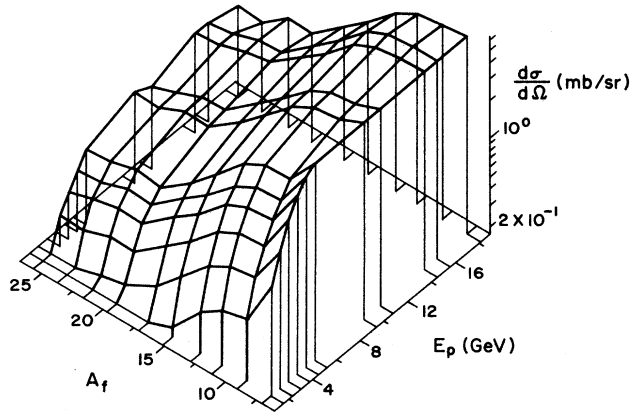

FIG. 2. Dependence of fragment yields at 48.5° on mass number and proton energy.

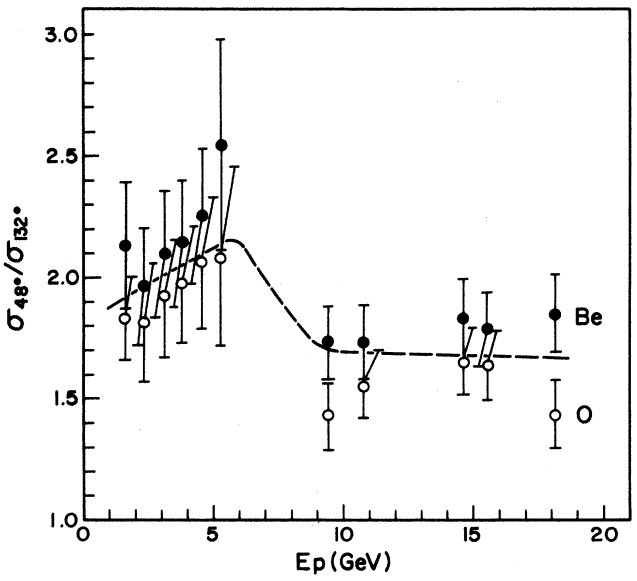

FIG. 4. Proton energy dependence of the ratio of differential cross sections at 48.5° and 131.5° of Be and O fragments.

IV. DISCUSSION

A. Thermal model fits to fragment energy spectra

In our previous Fermilab experiment,[6] we successfully fit the fragment kinetic energy spectra with an expression based on a thermal droplet model, in which fragment emission is pictured as a multibody breakup of the remnant with mass A_r formed in the initial proton-xenon interaction. The kinetic energy distribution consists of a convolution of two Maxwellian distributions averaged over a distribution of Coulomb repulsion energies, B. The high-energy Maxwellian is characterized by a slope parameter T_1 that reflects the nucleon mean-square momentum in the remnant system.[52] The low-energy Maxwellian is characterized by a slope parameter T_2. The fitting function is

$$\frac{d^2\sigma}{dE_{\rm lab}d\Omega}=N(E_{\rm lab}/E_{\rm c.m.})^{1/2}\int_0^{\min(E_{\rm c.m.},B_{\max})}P(B)dB \times\int_0^{E_{\rm c.m.}-B}\epsilon^{1/2}(E_{\rm c.m.}-B)^{1/2}\exp\left[\frac{-\nu\epsilon}{T_1}\right]\exp\left[\frac{-\nu(E_{\rm c.m.}-B-\epsilon)}{T_2}\right]d\epsilon\ , \tag{1}$$

where N is an overall normalization constant, ν is a recoil correction factor, $\nu=(1-A_f/A_r)^{-1}$, ϵ is the energy associated with the high-energy Maxwellian, and the center of mass energy $E_{\rm c.m.}$ is

$$E_{\rm c.m.}=E_{\rm lab}+(\tfrac{1}{2})A_f\beta^2-2[E_{\rm lab}(\tfrac{1}{2})A_f\beta^2]^{1/2}\cos\theta\ . \tag{2}$$

The value of β was obtained from the kinematic shift in the spectra peaks obtained at the two values of the laboratory angle θ.

The distribution of Coulomb energies was obtained on the basis of a geometric model, in which the Coulomb energy of a fragment is assumed to depend on its position within the remnant at breakup.[6] By arguing that the probability to form a fragment at a particular point within the remnant is directly related to the remnant density distribution, assumed to be Gaussian, we parametrized the Coulomb probability distribution as

$$P(B)\propto\exp-\left[\frac{R^2}{2\sigma_R^2}\right]\ , \tag{3}$$

where R is the distance between the centers of the remnant and fragment at breakup. The standard deviation of the distribution, σ_R, is closely related to the most probable value of R. The center-of-mass fragment kinetic energy due to the Coulomb repulsion between the charge inside the fragment sphere and the rest of the system is[47]

$$B(R)=\frac{Z_rZ_fe^2}{R_r^3\nu^2}(R^2+3RR_f)\ , \tag{4}$$

where Z_r and R_r are the change and radius of the remnant, respectively, and Z_f and R_f are the corresponding quantities for the fragment. This expression assumes that the remnant and fragment have the same charge distribution. The radii were obtained on the basis of a nuclear radius parameter $r_0=1.2$ fm. The upper limit of the Coulomb energy integral in Eq. (1) represents the smaller of $E_{\rm c.m.}$ and $B_{\max}$, where $B_{\max}$ is simply $B(R)$ evaluated at $R_{\max}=R_r-R_f$. The present formulation of Coulomb smearing adds just one adjustable parameter to the fit, i.e., σ_R.

The various spectra were fitted with Eq. (1) using the code MINUIT.[53] The parameters obtained from the fit to each spectrum are T_1, T_2, σ_R, and the overall normalization. The charge and mass of the remnant, $Z_r=48$ and $A_r=115$, were obtained from the fragment mass dependence of the slope parameter T_1, as described in detail in our previous work.[6]

The fitted curves have been compared with the spectra in Fig. 1. Additional comparisons are shown in Fig. 5. The parametrization based on our model gives excellent fits to the data obtained for proton energies above 9 GeV. The high-energy slope parameter T_1 is 15.6±0.5 MeV at 48.5°, and 12.0±0.4 MeV at 131.5°. Both values are independent of fragment charge and proton energy over the entire energy regime. This can be seen in Fig. 6, which shows a semilog plot of the spectra of N and F fragments as a function of proton energy, focusing on the high-energy tails. The constancy of the slopes demonstrates that T_1 is independent of incident proton energy. This fact reinforces the notion that T_1 is nonthermal in origin.

The values of T_2 also are independent of fragment Z and proton energy (above 9 GeV). The values obtained at 48.5° and 131.5° are 2.2±0.2 MeV and 4.4±0.5 MeV, respectively. (The values for Li fragments are ~4 MeV at both angles.) The values of the most probable Coulomb energy, B_{mp}, i.e., the Coulomb energy evaluated at the most probable location of the fragment within the remnant at breakup, were obtained from the fitted values of σ_R and are plotted as a function of fragment charge in Fig. 7. The values are small ($\lesssim 30\%$) compared to the tangent-spheres values, as expected from the assumed multibody nature of the breakup.

The values of β obtained from the kinematic shift in the spectra are plotted versus proton energy in Fig. 8. Since there is no discernible trend with Z_f, we have averaged the results obtained for individual fragments. The values of β increase with proton energy up to $E_p\sim 3$ GeV and decrease at higher energies. Evidently, the longitudinal momentum transferred to the remnant in the initial interaction peaks at ~3 GeV. This behavior is qualitatively similar to that displayed by the ratio of fragment

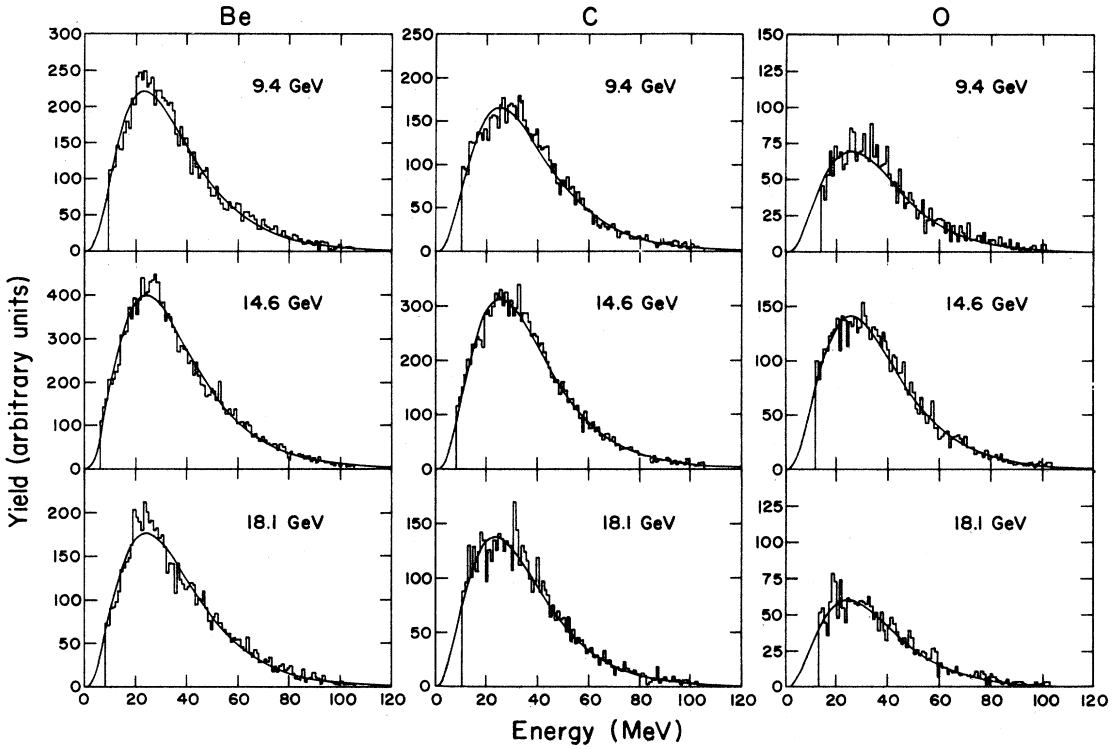

FIG. 5. Droplet model fits (curves) to the energy spectra of Be, C, and O fragments (histograms) emitted in reactions induced by ≥ 9 GeV protons. The proton energies are indicated.

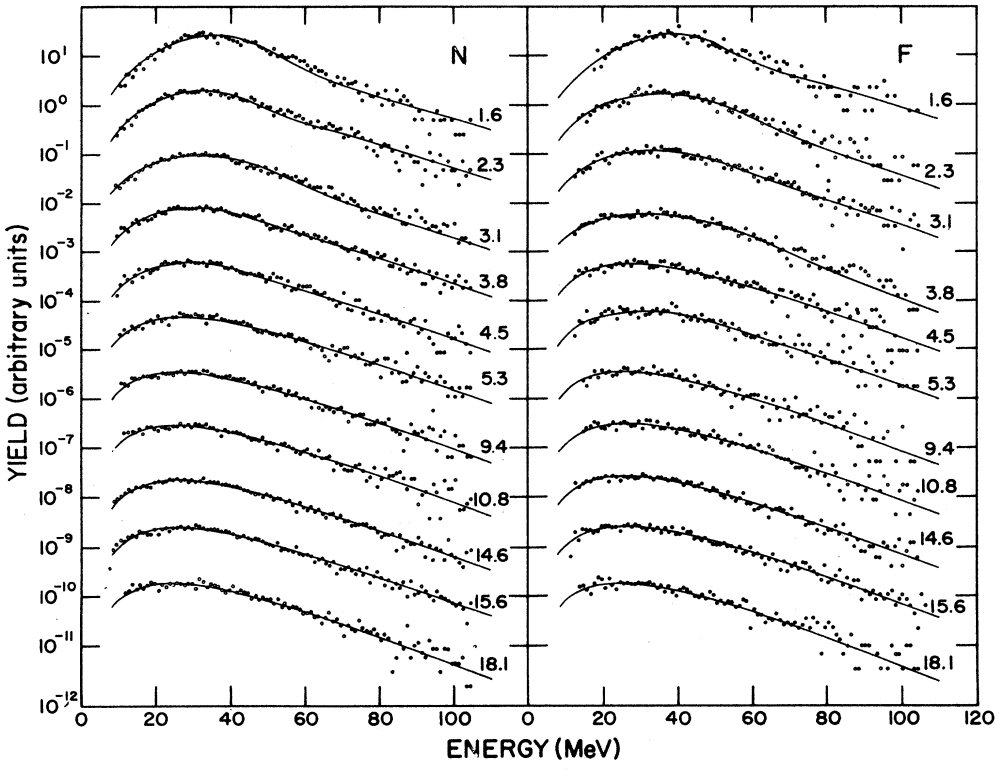

FIG. 6. Semi-log plot of the spectra of N and F fragments at the indicated proton energies, emphasizing the high-energy tails. The curves through the experimental points above 9 GeV represent the thermal model fit. Below 6 GeV, the curves are obtained from the combined parametrization described in Sec. IV B.

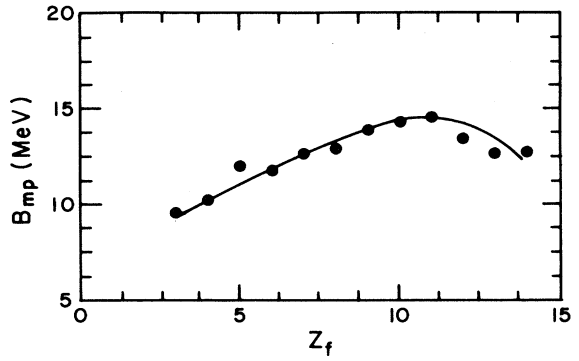

FIG. 7. Dependence of most probable fragment Coulomb energy B_{mp} on fragment Z.

yields at forward and backward angles, and has been observed in previous studies.[31,50,51] We defer further discussion of the β values to Sec. IV C.

B. A second mechanism at low proton energies

Figure 9 extends the comparison of the fragment energy spectra with the droplet model to proton energies below 6 GeV.[54] The curves were obtained with the same numerical values of the parameters as the higher energy fits. With decreasing proton energy, the peak narrows appreciably and the low-energy side of the spectra becomes somewhat concave. However, as already noted in Fig. 6, the high-energy tails have the same slope as at higher energies. As shown in the figure, we were unable to fit these data with the parametrization of Eq. (1). To explore whether changes in the parameters of the model could lead to acceptable fits, we allowed all four parameters in Eq. (1) to vary freely. The results are shown in Fig. 10. Note that the calculated curves underestimate the peak intensity but overestimate the yield of both low- and high-energy fragments. In addition, the fitted peak energy is too low. The reduced χ^2 value for the best of these fits is ~ 15 compared to values of ~ 1.5 for the higher proton energy fits.

The discrepancy suggests that a second mechanism may be contributing to the fragment yields at low energies. Indeed, there is both theoretical and experimental evidence for fragment emission in a binary process at intermediate energies. Moretto[55] has described fragment emission as part of the continuum of statistical breakup processes ranging from evaporation to binary fission. The predicted kinetic energy spectra change from Maxwellian to Gaussian with increasing fragment charge and mass. More recently, Gross *et al.*[24] examined the decay channels of hot nuclei on the basis of a statistical microcanonical model. These workers find that binary breakup should give way to multifragmentation at excitation energies attainable in the collision of GeV protons with nuclei. The experimental evidence indicates that in intermediate-energy heavy-ion reactions light fragment emission is the result of a binary process.[56–59] However, at higher energies fragment emission involves a multibody breakup.[10] Furthermore, the spectra of light fragments with $Z \geq 5$ emitted in intermediate-energy reactions are symmetric and Gaussian-like,[59] in accord with the predictions.[55]

In view of these results, we have assumed that the discrepancy depicted in Figs. 9 and 10 reflects the additional contribution of a binary breakup process. As noted above, the energy spectrum of fragments emitted in this process can be characterized by a Gaussian,

$$\frac{d^2\sigma_b}{dE_{\rm lab}d\Omega} = N_b \exp\left[-\frac{(E_{\rm lab}-E_0)^2}{2\sigma_b^2}\right] . \quad (5)$$

The spectra obtained for 1.3–5.6 GeV protons were fitted with the sum of Eqs. (1) and (5). The most accurate determination of the relative contribution of the two mechanisms was made by minimizing the number of fitted parameters. Since the values of T_2 and σ_R were found to be virtually independent of energy and fragment Z above 9 GeV, we used the average values obtained at these energies to fit the spectra below 6 GeV. In addition, we have already noted the constancy of T_1 over the entire proton energy regime covered in this experiment. Thus there are only four free parameters, the two normalizations, E_0 and σ_b.

Figure 11 shows the resulting fits to the spectra displayed in Fig. 9. The combined parametrization gives an excellent fit to the data obtained for all fragments at both forward and backward angles. The values of χ^2 per degree of freedom are ~ 1.5, a factor of 10 lower than those for the fits based on the multibody breakup model alone.

Figure 12 shows the dependence on proton energy of the fractional contribution of the multibody breakup pro-

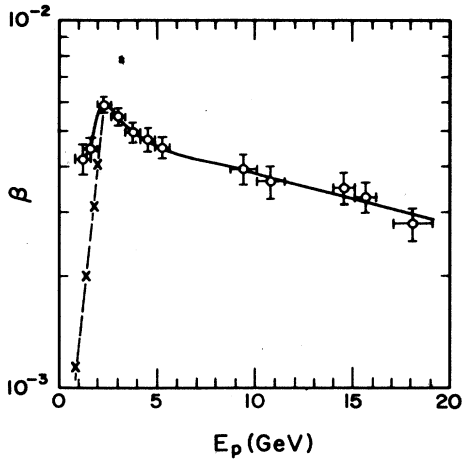

FIG. 8. Proton energy dependence of the velocity β of the remnant. The crosses are the result of a moving source calculation described in the text.

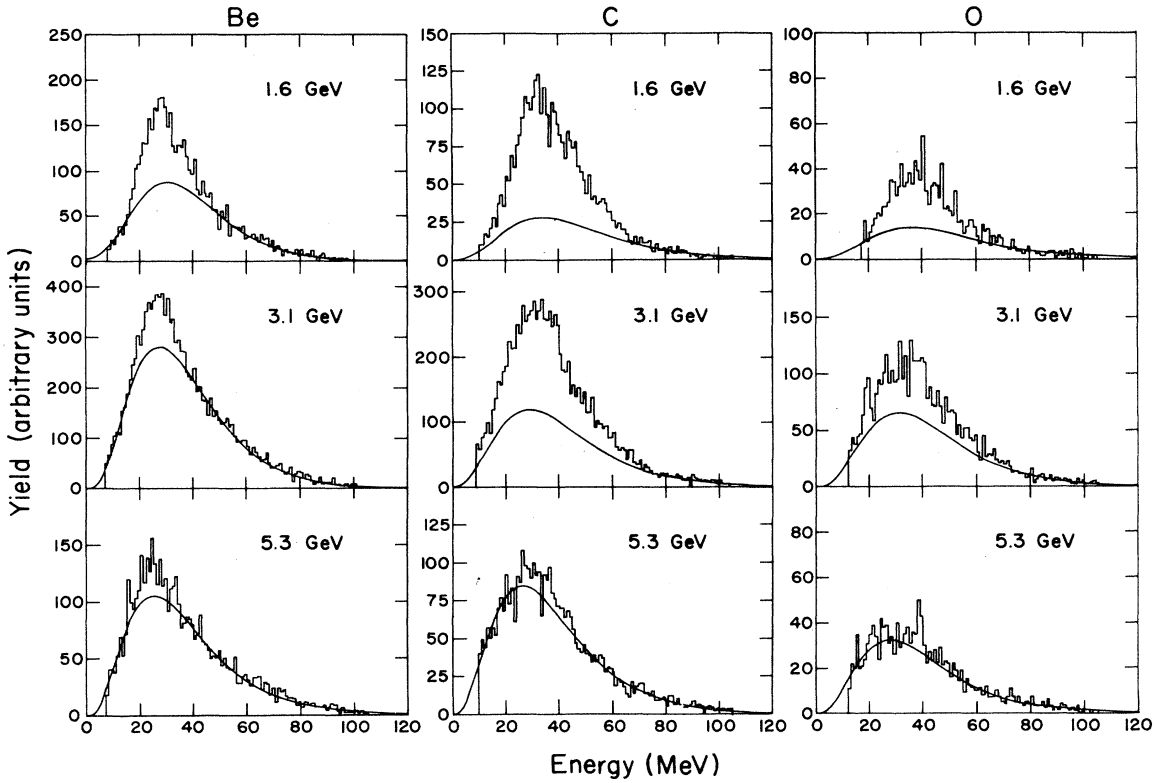

FIG. 9. Energy spectra of Be, C, and O fragments emitted in reactions induced by ≤ 6 GeV protons. The curves are based on the thermal model. The parameters (except for β) have the same values as those used at higher energies (see Fig. 5).

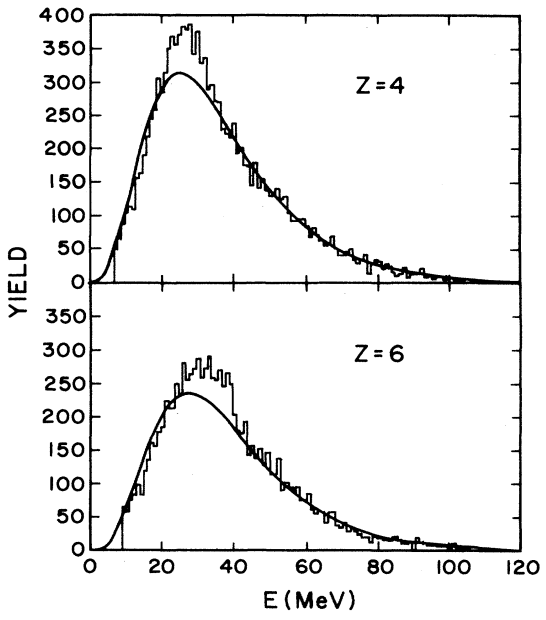

FIG. 10. Best fits of Eq. (1) to energy spectra of Be and C fragments obtained for $E_p = 2.7-3.4$ GeV. All the parameters were allowed to vary freely.

cess to the total fragment yield at forward and backward angles. The results have been averaged over all fragments. The figure shows a definite increase in the multifragmentation fraction with energy, ranging from approximately 50% at 1.6 GeV to ~90% at 5.3 GeV, virtually independent of angle. The inclusion of a Gaussian component in the fits for $E_p > 9$ GeV gave a maximum contribution of 2% for this component. Figure 3 shows the excitation functions for the multifragmentation component. The cross sections drop steeply at low energies towards a threshold in the vicinity of 1 GeV and level off above 10 GeV. In contrast, the excitation functions for the binary component must have a substantially lower threshold and must either peak or level off at a few GeV.

Figure 13 shows the variation with fragment charge of the most probable energy E_0 of the Gaussian distribution, averaged over all proton energy intervals. In a binary breakup model, the most probable energy must be close in value to the Coulomb energy arising from the repulsion between the two fragments. We note that the values of E_0 show the expected increase with fragment Z and, for a given Z, are substantially larger than the most probable fragment Coulomb energies associated with the multibody breakup process, (see Fig. 7). This result supports our picture of the two mechanisms, since the breakup of a given remnant into two fragments should involve a higher Coulomb repulsion energy than its breakup into

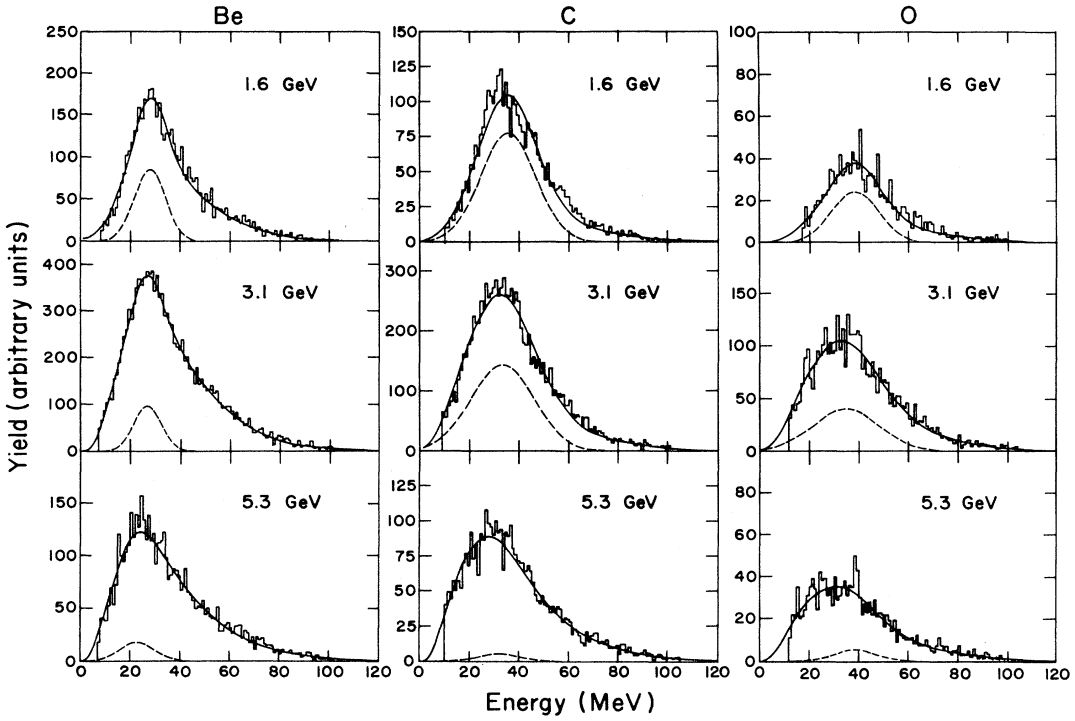

FIG. 11. Comparison of the energy spectra of Be, C, and O fragments emitted in reactions induced by ≤ 6 GeV protons (see Fig. 9) with multibody and two-body breakup models. The dashed curves show the separate contribution of two-body break up.

more than two fragments.

We have also parametrized the spectra of the binary component by a Maxwellian, since the fragment spectra reported by Green *et al.*[39] for the interaction of silver with 480 MeV protons are closer to being Maxwellian than Gaussian. Qualitatively similar results are obtained although the fits are not as good as those shown above.

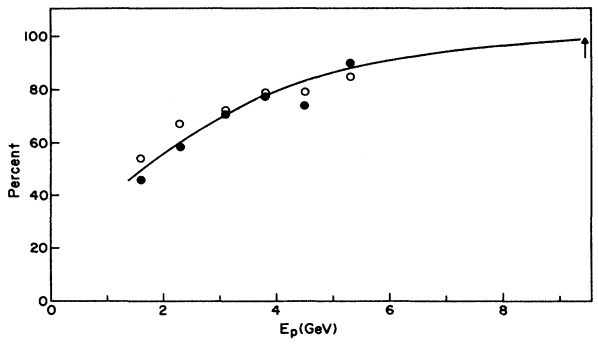

FIG. 12. Dependence on proton energy of the fractional contribution of multifragmentation to the fragment yields at 48.5° (open circles) and at 131.5° (solid circles). The arrow shows the lower limit of this contribution above 9 GeV.

C. Energy and momentum transfer in fragmentation

The results of our experiment indicate that IMF emission in proton reactions is a phenomenon observed primarily at GeV energies. It is of interest to examine the nature of the interaction of GeV protons with nuclei in order to determine which factors are responsible for the occurrence of fragmentation.

Figure 14 shows a comparison between a typical IMF excitation function and that for the *p-p* inelastic cross section. Both cross sections show a similar rapid rise with energy although the *p-p* cross section reaches a plateau by 2 GeV while the IMF cross section continues to rise until

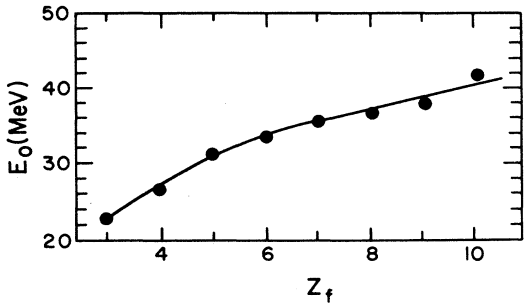

FIG. 13. Dependence on Z_f of the most probable energy E_0 of the Gaussian component.

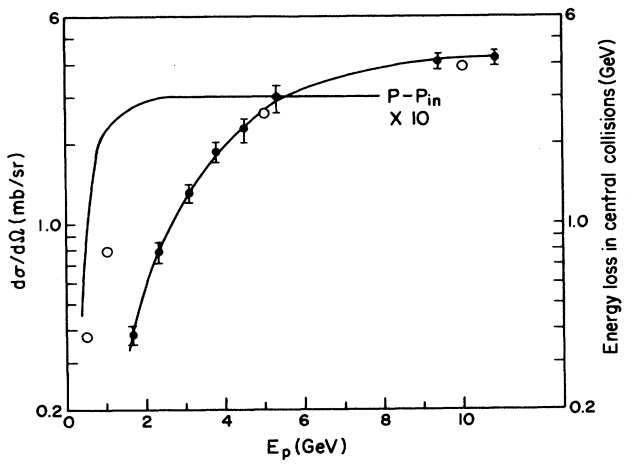

FIG. 14. Comparison of the energy dependence of IMF cross sections (solid circles), the p-p inelastic cross section, and the calculated (Ref. 60) energy loss in p-nucleus central collisions (open circles).

~ 10 GeV. This similarity in behavior, which was already noted in the early radiochemical studies of fragment emission,[30] suggests that inelastic nucleon-nucleon scattering plays an important role in initiating IMF emission.

A more detailed picture is provided by Cugnon,[60] who examined the energy loss of high-energy protons interacting with nuclei by means of an intranuclear cascade calculation. Cugnon finds that the number of collisions made by an incident proton in central collisions increases with bombarding energy up to ~ 10 GeV. Evidently, multiple p-nucleon inelastic collisions are of importance in this energy regime. These collisions provide an efficient mechanism for depositing energy in the nucleus. Thus, as shown in Fig. 14, the fragment excitation functions scale with the calculated energy loss in central collisions suggesting that fragmentation results from interactions in which the incident proton loses a large amount of energy in the target nucleus.

The variation with bombarding energy of β, the velocity of the remnant, can be examined in light of the results of Nakai and collaborators.[61] These workers find that in approximately 30% of the interactions of 1–4 GeV hadrons with nuclei the incident particle is stopped by the nucleus. About 75% of the incident energy is carried off by a moving source of nucleons and mesons leaving behind a highly excited remnant. The observed charged particle multiplicity is much higher in interactions of this type than in those in which a leading particle is emitted, indicating the occurrence of central collisions. Since multifragmentation occurs in high-multiplicity interactions,[10] we shall assume that fragment emission is associated with interactions in which there is a moving source. The size of the moving source ν is parametrized as

$$\nu=(3 \text{ to } 5)A_T^{1/3} , \tag{6}$$

and the average source velocity β_s is

$$\beta_s=\frac{p_{\text{inc}}}{E_{\text{inc}}+\nu M_n} , \tag{7}$$

where A_T is the target mass, p_{inc} and E_{inc} are the incident proton momentum and energy, and M_n is the nucleon mass. The value of β can be obtained from that of β_s by conserving the momentum between the moving source and the remnant

$$\beta=\beta_{\text{lab}}\left[\frac{A_r+A_s}{A_r}\right]-\beta_s\left[\frac{A_s}{A_r}\right] , \tag{8}$$

where A_s and A_r are the mass of the source and remnant, respectively, and β_{lab}, the velocity of the target-proton composite, is

$$\beta_{\text{lab}}=\frac{p_{\text{inc}}}{(A_T+1)M_n} . \tag{9}$$

Values of β were obtained by means of Eq. (8) with A_s obtained from the value of ν given in Eq. (6). The results are given by the crosses in Fig. 8. The values of β obtained from the moving source fits decrease more sharply with decreasing proton energy than the experimental values. The observed discrepancy is an indication that the moving source must decrease in size with decreasing proton energy. Thus, instead of a constant value of $\nu \sim 20$, as expected from Eq. (6), the data require that ν decrease monotonically to approximately four at the lowest energy.

The results of Nakai *et al.*[61] unfortunately do not extend to energies substantially higher than the peak in β. Thus, any discussion of the decrease in β with increasing proton energy observed beyond ~ 3 GeV is necessarily speculative. The observed behavior can be reproduced on the assumption that the incident proton "punches through" the nucleus in central collisions once its energy exceeds approximately 4 GeV. The values of β_{lab} would then decrease and, on the assumption that the size of the moving source saturates at this energy at the value given by Eq. (6), the values of β in Eq. (8) would decrease in a manner consistent with our data.

Comparison of Fig. 8 and Fig. 14 indicates that while the maximum momentum transfer associated with fragment emission occurs at $E_p \sim 3$ GeV, the excitation energy does not saturate until ~ 10 GeV. This difference may indicate that the captured spray particles associated with the ejection of fast particles increase in energy and/or number up to ~ 10 GeV.

D. The approach to criticality in multifragmentation

Multifragmentation has been described in the context of the liquid-gas phase transition.[1] In this section we show that the evolution of the multifragment yield with fragment mass and with bombarding energy can be understood in terms of the phase transition.

The description of a gas of noninteracting clusters in thermal equilibrium has been given by Fisher in his droplet model.[9] The number of clusters per unit volume con-

taining n constituents depends on the Helmholtz free energy of the cluster, f_n, the chemical potential per particle, μ, and the temperature, T, as

$$\rho_n = \rho_0 n^{-\tau} \exp[-(f_n - \mu n)\beta] , \quad (10)$$

where $\beta = 1/k_B T$. The free energy contains contributions from both the volume and surface free energy of the droplets. Separating the bulk and surface terms, we can write Eq. (10) as[9]

$$\rho_n = \rho_0 n^{-\tau} X^{n^\sigma} Y^n . \quad (11)$$

The factor X arises from the surface free energy of the droplet; Y contains the volume free energy and the chemical potential. The critical point, $T = T_c$, $\rho = \rho_c$, occurs when $X = Y = 1$. Below the critical point, $X < 1$ and $Y > 0$. The liquid-gas coexistence curve corresponds to $Y = 1$; when $Y > 1$ the vapor is supersaturated. The temperature dependence in Eq. (11) is contained in X and Y. The parameter ρ_0 gives an overall normalization; τ and σ are critical exponents.

Although the droplet formula was derived in the thermodynamic limit of infinite particle number, we shall apply it to a case in which $n \sim 100$. As such, it is not strictly correct to speak of a sharp phase transition.[11] The effects of finite particle number on T_c have been explored for $N = Z$ systems with no Coulomb force. For a system of 100 particles, $T_c(100) \sim 0.75\ T_c(\infty)$.[62] The Coulomb force is predicted to be responsible for a further reduction of, perhaps, a few MeV.[62]

Equation (11) was used to fit the cross sections ascribed to multifragmentation on the assumption that the cross section for producing a fragment is proportional to ρ_n, the number of fragments of a given nucleon number per unit volume. For each of the 11 proton energy bins there corresponds a value of X and a value of Y determined from the fit. A single value of the overall normalization factor was used. In addition, τ was fixed at 2.2 and σ at 0.64, the experimental values for a liquid-gas phase transition.[63] For each of the 11 data sets, forward and backward, ten data points were fit with the two adjustable parameters, X and Y. The results of the two sets differ only in the value of the overall normalization constant. Therefore, in what follows, we will concentrate on the forward angle data.

The comparison between the fit and the data can be presented in two ways, i.e., $d\sigma/d\Omega$ vs E_p at a given A_f, or $d\sigma/d\Omega$ vs A_f at a given E_p. Figure 15 shows some typical excitation functions. It is clear that the fitted curves reproduce the general trends in the data. Figure 16 shows the variation of $d\sigma/d\Omega$ with A_f at the various proton energies. Once again, good fits are obtained. Thus, the droplet model can simultaneously fit both the energy and mass dependence of the fragment yields. To be sure, there are some systematic deviations from the curves in Fig. 16. For example, the data points corresponding to carbon lie above the fitted curves for all 11 bins. However, it must be remembered that Eq. (11) assumes a slowly varying binding energy per particle as a function of constituent number and a single type of constituent particle.[9] Since neither of these assumptions is valid for nuclei, some deviations are to be expected. Deexcitation of the primary fragments by evaporation leads to additional changes in the mass yield distribution. However, Fields *et al.*[64] have shown that these effects be-

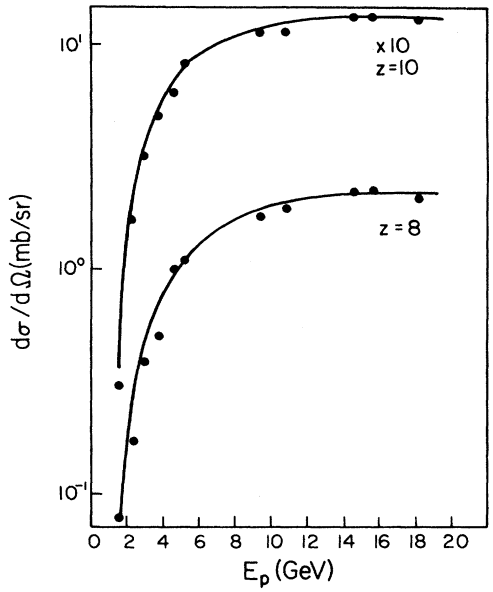

FIG. 15. Droplet model [Eq. (11)] fit to the energy dependence of multifragmentation cross sections of O and Ne fragments emitted at 48.5°.

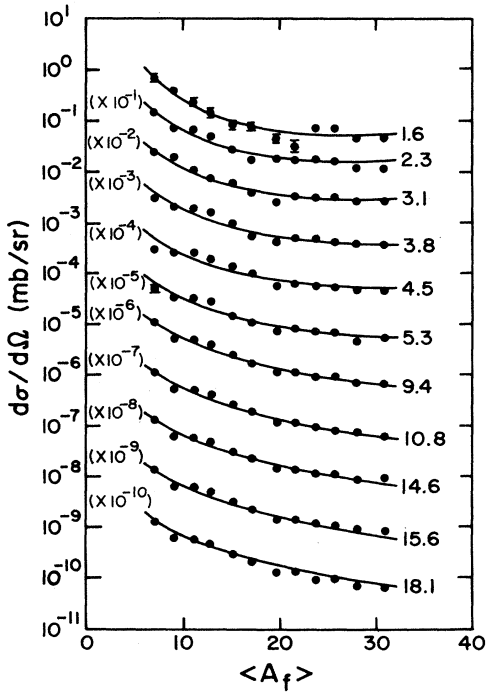

FIG. 16. Droplet model [Eq. (11)] fit to the mass dependence of multifragmentation cross sections of fragments emitted at 48.5°. The proton energies are indicated.

come negligible for $A_f \geq 10$.

The values of X and Y obtained from the fitting procedure are shown as a function of proton energy in Fig. 17. The uncertainties in these parameters were estimated by means of the Monte Carlo method. Using the multifragmentation cross sections obtained in Sec. IV B as input, new data sets were generated on the assumption of a Gaussian distribution for each cross section, with a mean equal to the input value and a standard deviation equal to its uncertainty. These uncertainties were obtained by combining in quadrature the statistical errors, the uncertainties in the extrapolation of the spectra to zero energy, and the uncertainties in the subtraction of the binary component. The overall random error ranged from approximately 7 to 17%. Systematic errors were not included because they affect only the cross section scale. Each generated data set was fitted with Eq. (11) and the values of X and Y were obtained The results of ten iterations were averaged, yielding mean values essentially identical to those shown in Fig. 17 and standard deviations of approximately 1%.

Figure 17 shows the X increases with proton energy and Y displays the opposite behavior. Interestingly, both X and Y approach unity above 10 GeV, where fragment production enters the limiting fragmentation region. This result is independent of the overall normalization. Within the context of the droplet model, we can conclude that the temperature of the fragmenting system increases with E_p and approaches the critical value at ~ 10 GeV.

Our analysis indicates that the liquid-gas critical region may be reached at a proton energy above 10 GeV. How are fragments produced at lower energies? This question can be examined with the help of a phase diagram of nuclear matter. Figure 18 shows a phase diagram obtained with an equation of state derived from a zero-range Skyrme-type interaction.[15] Our results can be viewed in terms of this diagram on the assumption that reaction trajectories leading to fragmentation follow the isentropic expansions shown by the dashed lines.[12,15] To do so we must estimate the entropy generated in interactions leading to fragment production as a function of proton energy. However, to evaluate the entropy, we must first estimate the excitation energy of the remnant.

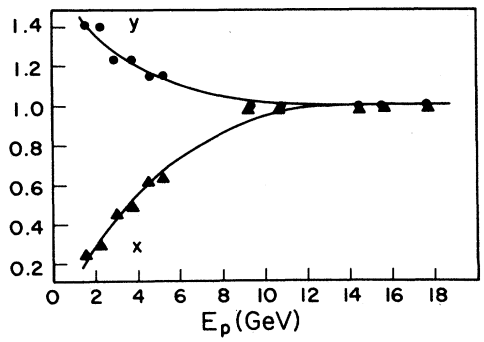

FIG. 17. Proton energy dependence of the parameters X and Y obtained from the fit of Eq. (11).

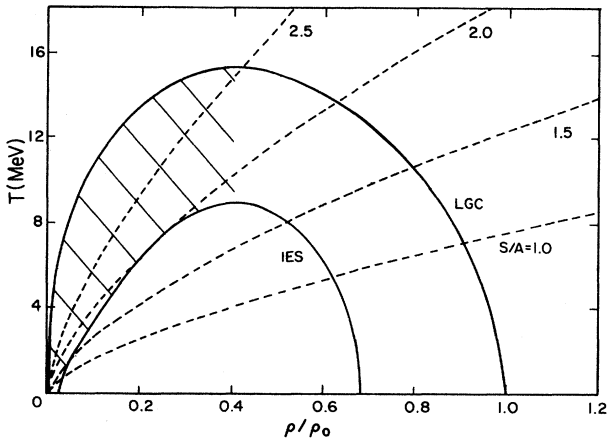

FIG. 18. Phase diagram of nuclear matter. Liquid-gas coexistence (LGC) curve; isentropic spinodal (IES). The dashed curves represent isentropic trajectories for the indicated values of S/A. The hatched area is the metastable region of supersaturated vapor.

As already noted, Nakai *et al.*[61] have shown that central collisions of 1–4 GeV protons with nuclear targets lead to the forward emission of a "moving source" of energetic particles, which on average carries away some 75% of the incident kinetic energy. The remaining 25% of the energy is deposited as excitation energy in the residual nucleus, which is somewhat reduced in nucleon number. Thus, we estimate that the remnant of a 4 GeV p-Xe central collision has an excitation energy E^* of about 1 GeV, or about 8–9 MeV/nucleon.

An independent estimate of this value can be obtained from a recent simulation of central collisions,[65] which showed that the multifragment mass yield distribution for a given proton energy can be parametrized as

$$\text{Yield}(A_f) \propto A_f^{-\tau'} . \tag{12}$$

Comparison with Eq. (11) shows that the temperature dependence of X and Y has been incorporated in the value of an effective power law exponent τ'. It has been argued[65] that a plot of τ' vs E_p should go through a minimum at an energy for which the average excitation energy is equal to the total binding energy of the nucleus, i.e., ~ 0.9 GeV for the remnant of a p-Xe interaction. We have fit Eq. (12) to our data and show the variation of τ' with E_p in Fig. 19. The uncertainties in τ' were estimated in the same way as those in X and Y, and were found to be $\sim 5\%$. A minimum is observed at $E_p \sim 4$ GeV, and τ' levels off at ~ 2.1 at high energies. We conclude that at $E_p \sim 4$ GeV, $E^* \sim 0.9$ GeV, in agreement with the value derived from Nakai *et al.*[61]

The agreement between these two independent estimates of E^* encourages us to use the Nakai estimates of this quantity for $E_p = 1$–4 GeV. Values of initial T and S/A can be derived from E^* on the basis of the Fermi gas model: $E^* = A_r T_i^2/10$ and $S/A = T_i/5$. At the

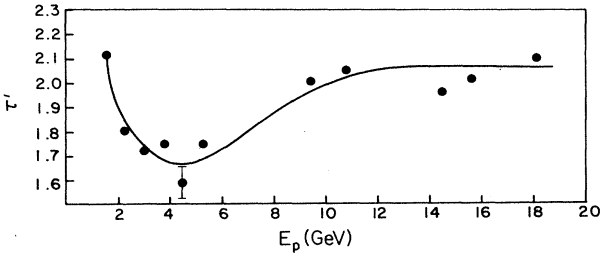

FIG. 19. Dependence of effective power law exponent τ' on proton energy. The curve is drawn to guide the eye.

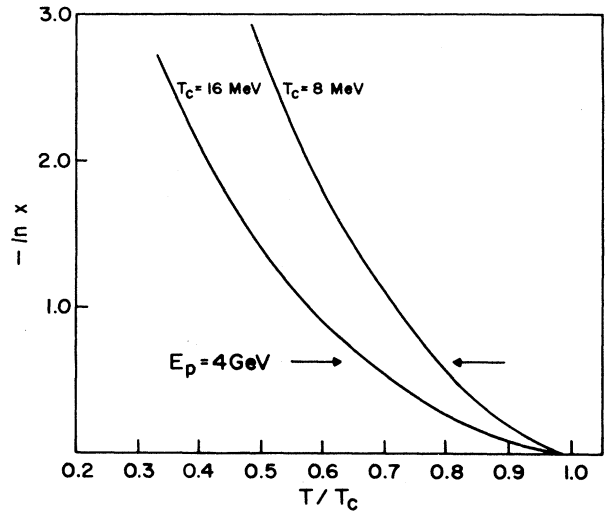

FIG. 20. The surface free energy $-\ln X$ vs T/T_c for two choices of T_c, 8 MeV and 16 MeV. The arrows mark the value of $-\ln X$ at 4 GeV.

lowest proton energy, 1.6 GeV, we estimate $E^*=400$ MeV, and obtain $T_i \sim 6$ MeV and $S/A \sim 1$. Figure 18 shows that at these low entropies the isentropic spinodal is reached and fragmentation can occur in the mechanical instability region.[12] However, the fragment production cross sections are only $\sim \frac{1}{10}$ of their limiting value, indicating that this process is not very probable. The estimated value of T_i compares favorably with experimental[66,67] and calculated[23] values of the temperature at which the binary breakup of a compoundlike nucleus gives way to multifragmentation. Our observation of a change in mechanism at these low energies also is in accord with these temperature estimates.

At $E_p \sim 4$ GeV, we estimate $S/A \sim 2$. Figure 18 shows that a reaction trajectory with this S/A value can reach the metastable phase of supersaturated vapor. Fragment formation then corresponds to droplet formation in a supersaturated vapor ($Y > 1$).[11]

The change in T and S/A as the beam energy increases from 4 GeV to the limiting fragmentation region can be estimated as follows. The parameter X is related to the surface properties of a drop at temperature T by[11]

$$-\ln(X)=\frac{18}{T}\left[1+\frac{3}{2}\frac{T}{T_c}\right]\left[1-\frac{T}{T_c}\right]^{3/2}. \quad (13)$$

At $E_p=4$ GeV the value of X is approximately 0.53 while in the limiting fragmentation region $X \sim 1$. Figure 20 shows a plot of $-\ln(X)$ vs T/T_c for two choices of T_c, 8 MeV, and 16 MeV. We see that T increases by between 25% and 40% in going from $E_p=4$ GeV to $E_p > 10$ GeV, depending on the choice of T_c. The entropy per nucleon increases by the same factor to $S/A \sim 2.6$–2.8. Figure 18 shows that a trajectory with S/A of this magnitude passes through the critical region. Thus, entropy estimates in conjunction with the phase diagram support the conclusion based on the limiting values of X and Y that fragmentation can be described as a critical phenomenon for incident proton energies above ~ 10 GeV.

The value of τ' obtained above 10 GeV, $\tau' \sim 2.1$ (see Fig. 19), is significantly smaller than the value $\tau'=2.6$ previously obtained at Fermilab energies.[6] The discrepancy reflects, in part, the fact that in the Fermilab experiment we measured a true fragment mass distribution whereas in the present work we use an effective mass distribution in which the average value of A_f for each Z_f was obtained from the isotopic yield distribution determined at Fermilab.[6] The analysis of the Fermilab data by this same approach reduces τ' from 2.6 to 2.3. The remaining discrepancy may be the result of the large difference between AGS and Fermilab energies and of the difference in the angles at which fragment emission was detected in the two experiments.

In a recent publication Panagiotou *et al.*[68] presented a plot similar to that in Fig. 19 based on differential cross sections for IMF production in the interaction of silver with 0.21–0.48 GeV and 4.9 GeV protons,[37–39] and on our earlier xenon data for 80–300 GeV protons.[6] These workers observed a decrease in τ' between 0.21 and 4.9 GeV followed by a higher value at 80 GeV. Although the use of data obtained from different targets at various angles, covering different mass intervals and involving a combination of mechanisms, has been criticized,[69] the results appear to be consistent with the much more closely spaced data reported here. Panagiotou *et al.*[68] propose that the observed energy dependence of τ' may indicate that the nucleus has reached the critical temperature at the bombarding energy corresponding to the minimum in τ'. Our more complete analysis shows that this is not the case. The energy dependence of τ' is determined by the interplay of surface and volume effects and thus by the combined effect of the parameters X and Y as a function of energy. The critical regime is attained only when these parameters become equal to unity. As already shown in Fig. 17, this does not occur for proton-xenon interactions at the energy at which τ' goes through a minimum.

In an attempt to extract the critical temperature from literature data, Panagiotou *et al.*[68] examined the variation of the effective power law exponent τ' with the tem-

perature of the emitting system. These workers assumed that the temperature is obtainable from the slope of the high-energy tails of spectra (i.e., the temperature is given by T_1, in our notation). However, as discussed in Sec. IV A, T_1 is believed to be a measure of the nucleon mean-square momentum rather than of the temperature. Consequently, the validity of their analysis is questionable.

V. CONCLUSIONS

The use of an internal xenon gas jet target at the AGS has enabled us to make a detailed study of the energy dependence of IMF production in the 1–19 GeV proton energy regime. The cross sections for IMF emission increase sharply with energy up to ~10 GeV and become nearly constant at higher energies. The observed energy dependence resembles that of the calculated energy loss in p-nucleus central collisions, which in turn is determined primarily by the effect of multiple inelastic p-nucleon collisions. The observed energy dependence of the longitudinal momentum of the remnant is consistent with an adaptation of the moving source model.[61] The data require that the size of the moving source increase with energy up to ~4 GeV and that the incident proton punch through the nucleus at higher energies.

The IMF energy spectra were fit with a four-parameter function based on the thermal droplet model, consisting of two convoluted Maxwellians averaged over a distribution of Coulomb energies. Excellent fits to the data were obtained at proton energies above 9 GeV. However, below 6 GeV the spectra show the presence of a second component, assumed to be Gaussian, which makes an increasing contribution with decreasing proton energy. Evidence is presented to support the hypothesis that the Gaussian component is the result of a binary breakup process while the Maxwellian component results from multifragmentation. The latter process has a threshold in the vicinity of 1 GeV and becomes the dominant mechanism at a few GeV. The emission of IMF below GeV energies must, in this view, be due to binary breakup. The cross section for this process must peak or become constant at a proton energy of no more than a few GeV.

The simultaneous evolution of the multifragmentation component with mass and energy has been successfully described by the Fisher droplet model. This model indicates that fragmentation may be interpreted as a critical phenomenon at bombarding energies above approximately 10 GeV. Our analysis in terms of the phase diagram of nuclear matter indicates that cross sections for fragment production become appreciable when the entropy generated in the target is a significant fraction of the limiting entropy for a system of finite particle number. We find that, with increasing proton energy, multifragmentation occurs first in the mechanical instability region, then in the supersaturated vapor, and finally, above 10 GeV, in the critical region. The occurrence of criticality at the energy for which the regime of limiting fragmentation is reached is a remarkable coincidence, the implications of which remain to be addressed.

ACKNOWLEDGMENTS

We would like to thank the members of the Alternating Gradient Synchrotron (AGS) Division at Brookhaven National Laboratory and express our gratitude to A. Pendzick, J. Tuozzolo, H. Hseuh, R. Skelton, J. Glenn, M. Zguris, H. Foelsche, and especially to K. Reece and the other operators in the AGS main control room for their assistance during the jet target facility installation and operation. We acknowledge useful discussions with Y. E. Kim, P. F. Muzikar, and H. Nakanishi. This work was supported by the U.S. Department of Energy.

*Present address: Hayllym University, Dept. of Chemistry, 1-Okchun-Dong, Chooncheon, Korea 200.

†Present address: Mission Research Corporation, 4935 N. 35th St., Colorado Springs, CO 80919.

‡Present address: Lawrence Livermore Laboratory, P.O. Box 808, MS 1-208, Livermore, CA 94550.

[1]J. E. Finn, S. Agarwal, A. Bujak, J. Chuang, L. J. Gutay, A. S. Hirsch, R. W. Minich, N. T. Porile, R. P. Scharenberg, B. C. Stringfellow, and F. T. Turkot, Phys. Rev. Lett. **49**, 1321 (1982).

[2]C. S. Kiang, Phys. Rev. Lett. **24**, 47 (1970).

[3]H. E. Stanley, *Phase Transitions and Critical Phenomena* (Oxford University, New York, 1971).

[4]D. Stauffer, Phys. Rep. **54**, 1 (1979).

[5]R. W. Minich, S. Agarwal, A. Bujak, J. Chuang, J. E. Finn, L. J. Gutay, A. S. Hirsch, N. T. Porile, R. P. Scharenberg, B. C. Stringfellow, and F. Turkot, Phys. Lett. **118B**, 458 (1982).

[6]A. S. Hirsch, A. Bujak, J. E. Finn, L. J. Gutay, R. W. Minich, N. T. Porile, R. P. Scharenberg, B. C. Stringfellow, and F. Turkot, Phys. Rev. C **29**, 508 (1984).

[7]A. S. Hirsch, A. Bujak, J. E. Finn, L. J. Gutay, R. W. Minich, N. T. Porile, R. P. Scharenberg, B. C. Stringfellow, and F. Turkot, Nucl. Phys. **A418**, 267c (1984).

[8]N. T. Porile, A. Bujak, J. E. Finn, L. J. Gutay, A. S. Hirsch, R. W. Minich, G. Paderewski, R. P. Scharenberg, B. C. Stringfellow, and F. Turkot, Phys. Lett. **156B**, 177 (1985).

[9]M. E. Fisher, Physica (N.Y.) **3**, 255 (1967); Rep. Prog. Phys. **30**, 615 (1967).

[10]A. I. Warwick *et al.*, Phys. Rev. C **27**, 1083 (1983).

[11]A. L. Goodman, J. I. Kapusta, and A. Z. Mekjian, Phys. Rev. C **30**, 851 (1984).

[12]J. A. Lopez and P. J. Siemens, Nucl. Phys. **A431**, 728 (1984).

[13]G. Fai *et al.*, Phys. Lett. **164B**, 265 (1985).

[14]H. W. Barz *et al.*, Nucl. Phys. **A448**, 753 (1986).

[15]D. H. Boal and A. L. Goodman, Phys. Rev. C **33**, 1690 (1986).

[16]D. H. E. Gross *et al.*, Z. Phys. A **309**, 41 (1982).

[17]G. Fai and J. Randrup, Nucl. Phys. **A381**, 557 (1982).

[18]W. A. Friedman and W. G. Lynch, Phys. Rev. C **28**, 950 (1983).

[19]D. H. Boal, Phys. Rev. C **28**, 2568 (1983).

[20]J. Aichelin, J. Hufner, and R. Ibarra, Phys. Rev. C **30**, 107 (1984).

[21]X. Campi, J. Desbois, and E. Lipparini, Phys. Lett. **124B**, 8 (1984).
[22]W. Bauer *et al.*, Phys. Lett. **150B**, 53 (1985).
[23]J. P. Bondorf *et al.*, Nucl. Phys. **A443**, 321 (1985).
[24]D. H. E. Gross *et al.*, Phys. Rev. Lett. **56**, 1544 (1986).
[25]T. S. Biro, J. Knoll, and J. Richert, Nucl. Phys. **A459**, 692 (1986).
[26]L. P. Csernai and J. I. Kapusta, Phys. Rep. **131**, 223 (1986).
[27]R. J. Lenk and V. R. Pandharipande, Phys. Rev. C **34**, 177 (1986).
[28]C. R. Grant, Phys. Rev. C **34**, 1950 (1986).
[29]B. J. Strack, Phys. Rev. C **35**, 691 (1987).
[30]R. Wolfgang *et al.*, Phys. Rev. **103**, 394 (1956).
[31]Ø, Scheidemann and N. T. Porile, Phys. Rev. C **14**, 1534 (1976).
[32]L. P. Remsberg and D. G. Perry, Phys. Rev. Lett. **35**, 361 (1975).
[33]D. R. Fortney and N. T. Porile, Phys. Rev. C **21**, 2511 (1980).
[34]D. R. Fortney and N. T. Porile, Phys. Rev. C **21**, 664 (1980).
[35]A. M. Poskanzer, G. W. Butler, and E. K. Hyde, Phys. Rev. C **3**, 882 (1971).
[36]E. K. Hyde, G. W. Butler, and A. M. Poskanzer, Phys. Rev. C **4**, 1759 (1971).
[37]G. D. Westfall *et al.*, Phys. Rev. C **17**, 1368 (1978).
[38]R. E. L. Green and R. G. Korteling, Phys. Rev. C **22**, 1594 (1980).
[39]R. E. L. Green, R. G. Korteling, and K. P. Jackson, Phys. Rev. C **29**, 1806 (1984).
[40]J. Gaidos *et al.*, Phys. Rev. Lett. **42**, 82 (1979).
[41]T. C. Sangster, A. T. Bujak, D. D. Carmony, Y. H. Chung, L. J. Gutay, A. S. Hirsch, M. Mahi, G. L. Paderewski, N. T. Porile, R. P. Scharenberg, and B. C. Stringfellow, Phys. Lett. B **188**, 29 (1987).
[42]N. T. Porile, A. T. Bujak, D. D. Carmony, Y. H. Chung, L. J. Gutay, A. S. Hirsch, M. Mahi, G. L. Paderewski, T. C. Sangster, R. P. Scharenberg, and B. C. Stringfellow, Nucl. Phys. **A471**, 149c (1987).
[43]M. Mahi, A. T. Bujak, D. D. Carmony, Y. H. Chung, L. J. Gutay, A. S. Hirsch, G. L. Paderewski, N. T. Porile, T. C. Sangster, R. P. Scharenberg, and B. C. Stringfellow, Phys. Rev. Lett. **60**, 1936 (1988).
[44]B. C. Stringfellow, A. T. Bujak, D. D. Carmony, Y. H. Chung, J. E. Finn, L. J. Gutay, A. S. Hirsch, M. Mahi, G. L. Paderewski, N. T. Porile, T. C. Sangster, R. P. Scharenberg, and F. Turkot, Nucl. Instrum. Meth. Phys. Res. **A251**, 242 (1986).
[45]A TOF mass identification system was included in each telescope. Unfortunately, the RF noise level in the main ring tunnel was too high to permit successful mass identification.
[46]D. M. Barrus and R. L. Blake, Rev. Sci. Instrum. **48**, 116 (1977).
[47]T. C. Sangster, Ph.D. thesis, Purdue University, 1986 (unpublished).
[48]J. W. Tippie and J. E. Kuluga, IEEE Trans. Nucl. Sci. **NS-24**, No. 1 (1977).
[49]C. F. Wang and N. T. Porile, Phys. Rev. C **34**, 1911 (1986).
[50]K. Beg and N. T. Porile, Phys. Rev. C **3**, 1631 (1971).
[51]S. B. Kaufman, E. P. Steinberg, and M. W. Weisfield, Phys. Rev. C **18**, 1349 (1978).
[52]A. S. Goldhaber, Phys. Lett. **53B**, 306 (1974).
[53]Program MINUIT, Computer Program Library (CERN, Geneva).
[54]Data could not be obtained at proton energies of 6–9 GeV because of beam instabilities associated with the AGS transition region.
[55]L. G. Moretto, Nucl. Phys. **A27**, 211 (1975).
[56]R. J. Charity, Nucl. Phys. **A471**, 225c (1987).
[57]R. J. Charity *et al.*, Phys. Rev. Lett. **56**, 1354 (1986).
[58]W. Mittig *et al.*, Phys. Lett. **154B**, 259 (1985).
[59]L. G. Sobotka *et al.*, Phys. Rev. Lett. **51**, 2187 (1983).
[60]J. Cugnon, Nucl. Phys. **A462**, 751 (1987).
[61]K. Nakai *et al.*, Phys. Lett. **121B**, 373 (1983).
[62]H. R. Jaquaman *et al.*, Phys. Rev. C **29**, 2067 (1984).
[63]J. C. LeGuillon and J. Zinn-Justin, Phys. Rev. B **21**, 3976 (1980).
[64]D. C. Fields *et al.*, Phys. Lett. B **187**, 257 (1987).
[65]T. J. Schlagel and V. R. Pandharipande, Phys. Rev. C **36**, 162 (1987).
[66]S. Song *et al.*, Phys. Lett. **130B**, 14 (1983).
[67]D. Fabris *et al.*, Nucl. Phys. **A471**, 351c (1987).
[68]A. D. Panagiotou, M. W. Curtin, and D. K. Scott, Phys. Rev. C **31**, 55 (1985).
[69]J. B. Cumming, Phys. Rev. C **32**, 1445 (1985).